

Using the Applied Element Method for Modelling Calcium-Silicate Brick Masonry Subjected to In-Plane Cyclic Loading

Daniele Malomo¹, Rui Pinho^{1,3}, Andrea Penna^{1,2}

¹Department of Civil Engineering and Architecture, University of Pavia, Via Ferrata 3, Pavia, 27100, Italy

²European Centre for Training and Research in Earthquake Engineering (Eucentre), Via Ferrata 1, Pavia, Italy

³Modelling and Structural Analysis Consulting (Mosayk Ltd.), Piazza Castello 19, Pavia, Italy

SUMMARY

The response of calcium-silicate unreinforced masonry construction to horizontal cyclic loading has recently become the focus of experimental and numerical research, given its extensive use in some areas of the world that are now exposed to induced earthquakes (e.g. north of the Netherlands). In order to assess the seismic behaviour of such construction, a relatively wide range of modelling methodologies are available, amongst which the discrete elements approach, which takes into account the intrinsic heterogeneity of a brick-mortar assembly, can probably be deemed as the most appropriate computational procedure. On the other hand, however, since discrete elements numerical methods are based on a discontinuum domain, often they are not able to model every stage of the structural response adequately, and because of the high computational burden required, the analysis scale should be chosen carefully. The Applied Element Method (AEM) is a relatively recent addition to the discrete elements family, with a high potential for overcoming the aforementioned limitations or difficulties. Initially conceived to model blast events and concrete structures, its use in the earthquake engineering field is, of late, increasing noticeably. In this paper, the employment of the AEM to model the in-plane cyclic response of calcium-silicate masonry walls is discussed and scrutinised, also through the comparison with experimental results of in-plane cyclic shear-compression tests on unreinforced masonry walls.

KEYWORDS: calcium-silicate; unreinforced masonry; numerical modelling; discrete elements; applied element method

1. INTRODUCTION

The Groningen region, in the north of the Netherlands, historically not prone to tectonic earthquakes, has in recent years been subjected to seismic events induced by reservoir depletion due to gas extraction (e.g. [1, 2]). Construction in this region is dominated by the presence of unreinforced masonry (URM) structures, a non-negligible portion of which features calcium-silicate bearing walls, which have thus now naturally become the focus of applied research endeavours aimed at assessing their response to horizontal seismic loading (e.g. [3]). The work described herein is part of such recent research efforts, and concerns the examination and verification, through comparison with experimental data, of a possible modelling strategy for the assessment of the in-plane cyclic response of the aforementioned calcium silicate walls.

Several modelling techniques of different levels of complexity and computational burden are available for reproducing analytically the behaviour of masonry structures. Simplified methods ranging from the application of Limit Analysis [3, 5, 6], to storey mechanism models [7, 8] have been employed over the years to study the seismic behaviour of masonry elements and buildings. Among these simplified procedures, Graziotti et al. [9] proposed an equivalent SDOF model for the evaluation of the global response of URM buildings using nonlinear dynamic analyses [10, 11]. Within a macro-modelling methodology, instead, homogenised finite masonry portions are assembled obtaining a global model with the aim to reduce computational efforts. Amongst other numerical approaches, the macroelement modelling strategy, typically implemented in equivalent-frame models, represents an acceptable compromise between accuracy and computational burden. In this regard, a wide range of contributions have been proposed (e.g., [12-16]). In order to decrease the approximation level, more refined numerical procedures, such as the Finite Element Method (FEM), have been adapted and applied to masonry structures, implementing nonlinear constitutive laws and by means of a material homogenization process. Two main numerical approaches are thus distinguished: the first one, based on a continuum idealisation, or macro-modelling, and the second one, which partially takes into account the system discontinuity, or micro-modelling. A comprehensive review of these methods can be found in Roca et al [17]. Nowadays, even though FEM is probably the most employed numerical tool, and extended or hybrid methods have been additionally implemented, phenomena such as block separation, rotation or frictional sliding are still extremely complicated to model. Approaches that intrinsically account for the discrete nature of masonry, have been also formalised since the early seventies [18]. According to the Discrete Element Method (DEM), the units, depending on the problem peculiarities, can be modelled as rigid (only interaction constitutive law is needed), pseudo-rigid, or deformable (continuum constitutive law must be included), replacing the real masonry arrangement without any meshing process [19, 20]. The

classical formulation of the DEM by Cundall and Hart [21] provides two main hypotheses, i.e. finite displacements and rotations modelling and an automatic detection of element contact/collision. However, it is noted that sometimes the borderline between FEM and DEM appears extremely blended in the light of other recent advancements (MDEM, EDEM, DEM/FEM), as accurately reported in Lourenço [22]. The DEM procedure is naturally well suited for collapse simulation, and thanks to this important feature a wide range of DEM versions have been developed, as discussed in what follows. Examples of successful applications to the seismic analysis of masonry structures can be found e.g. in De Lorenzis et al. [23] and in Tondelli et al. [24].

In order to improve contact and impact modelling, the Discontinuous Deformation Analysis (DDA) was initially proposed by Goodman [25] with the aim of solving geotechnical problems, anticipating the formulation of the Non-Smooth Contact Dynamics (NSCD), founded on similar principles and initially elaborated by Jean [26]. It involves an implicit time-stepping scheme in which blocks can be either rigid or deformable. Coulomb frictional phenomena between blocks are based on the work of Moreau [27], assuming unilateral contact. The NSCD method has been recently used to model the dynamic response of masonry structures, including numerical investigations on the in-plane behaviour of masonry walls [28, 29], arches [30] and analyses of historical masonry structures [31]. Notwithstanding the good results reported by the aforementioned researchers and the great potential of these discrete elements methods, their empirical formulation (e.g. the relationships between micro and macroscopic parameters, [32]), and the amount of data required to build a model often make them difficult to apply efficiently, even when dealing with simple structures. Furthermore, since most of the current available DEM codes are based on explicit numerical methods, the modelling of static or quasi-static phenomena is often computationally inefficient, requiring dynamic relaxation schemes and a proper calibration of the damping factors.

A different computational methodology, which partially overcomes these issues, characterises the rigid body spring model (RBSM), [33]. According to the latter, a masonry assembly is assumed to be composed of rigid blocks connected by discrete deformable interfaces with distributed normal and tangential nonlinear springs. The global response is obtained considering spring elongation and failures, which allows representing the final configuration of rigid block assembly. Although this approach was originally elaborated for handling static problems, some applications [34] have shown that, under several assumptions and considering relatively small structures, adequate results can be obtained even in the dynamic range. Meguro and Tagel-Din [35] proposed an analogous approach, the Applied Element Method (AEM), in which rigid units interact with each other through linear or nonlinear springs that represent the material properties. Whilst the RBSM often considers an additional spring at the joint level aimed at modelling the local rotational effects, in the AEM this contribution is accounted automatically assigning a different shear stiffness to the interface springs (thus decreasing the matrices dimensions). Another difference between these two similar methods is that, contrary to AEM, in most of the applications to masonry structures the RBSM element discretisation is based on an equivalent mesh, considering the influence of the unit arrangement by means of energy relations between the discrete (real) model and a representative homogenised macroscopic segment [36]. As demonstrated in [37], the Poisson effect is accounted intrinsically by the AEM, whereas the RBSM formulation requires additional degrees of freedom (DOFs) or the spring stiffness manipulation [38]. Finally, unlike the AEM [39], analysis up to complete collapse of a structure using RBSM is unattainable, since the latter does not consider the re-contact between neighbouring elements (if different from the ones initially set), as noted in [20, 40]. In this work, the employment of the AEM in the modelling of (calcium-silicate) masonry walls is further discussed and verified.

2. THE APPLIED ELEMENT METHOD AND THE MODELLING OF MASONRY STRUCTURES

2.1 Formulation overview

As mentioned above, according to the AEM procedure a given structure is modelled through discretisation in a virtual assembly of small rigid units, carrying only mass and damping of the system, connected by springs (see Figure 1, below).

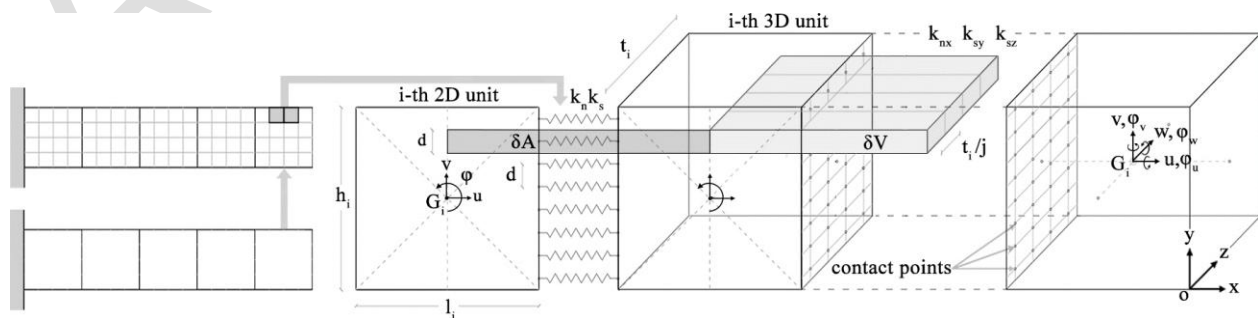


Figure 1. Multi-scale discretization of a plane element and domain influence of a set of springs in a 3-D space

The i -th plane unit is represented by a control point G_i , located in its geometrical centroid, and by a set of contact points that are uniformly distributed along the element edges. Two adjacent units are assumed to be connected at contact points by a pair of normal and shear springs (implemented with linear or nonlinear constitutive laws). Given that each group of springs completely describes stresses and deformations of a certain area δA , the behaviour of the whole assembly is deformable.

Each unit is characterised by three degrees of freedom (u, v, φ), representing its rigid body motion. Naturally, the total amount of degrees of freedom of a given model is $3n$, where n represents the number of units considered. Each normal, k_n , and shear, k_s , spring stiffness is quantified respectively using Eq. (1), which involve geometrical parameters, such as the length l_i and the thickness t_i , modelling values such as the distance d between two consequent springs, and the elastic material properties E (Young's modulus) and G (shear modulus).

$$k_n = \left(\frac{E d t_i}{l_i} \right), \quad k_s = \left(\frac{G d t_i}{l_i} \right) \quad (1) \quad k_{nx} = \sum_{i=1}^j \left(\frac{E_x d \left(\frac{t_i}{j} \right)}{l_i} \right), \quad k_{sy} = \sum_{i=1}^j \left(\frac{G_{xy} d \left(\frac{t_i}{j} \right)}{l_i} \right), \quad k_{sz} = \sum_{i=1}^j \left(\frac{G_{xz} d \left(\frac{t_i}{j} \right)}{l_i} \right) \quad (2)$$

As represented in Figure 1, if a number $j > 1$ of springs is arranged along the thickness t_i , the Eq. (1) now referred to a finite volume δV , can be extended to the three-dimensional case, becoming Eq. (2), where the subscripts x, y and z indicate the orientation with respect to the global coordinate system. Further details on the AEM formulation can be found e.g. in [41, 42], with the derivation of the stiffness matrix having been included in [43].

2.2 Formulation for masonry structures

Within the framework of AEM modelling of URM structures, an arbitrary masonry segment is composed of brick elements connected to each other by equivalent springs, in which the mechanical properties of brick-mortar interfaces (see Figure 2) are lumped (i.e. no additional DOFs are assigned to mortar layers). A given brick can be modelled as a rigid block or as an assembly of units; if it is desired to model potential splitting or crushing of bricks, then the latter need necessarily to be discretised).

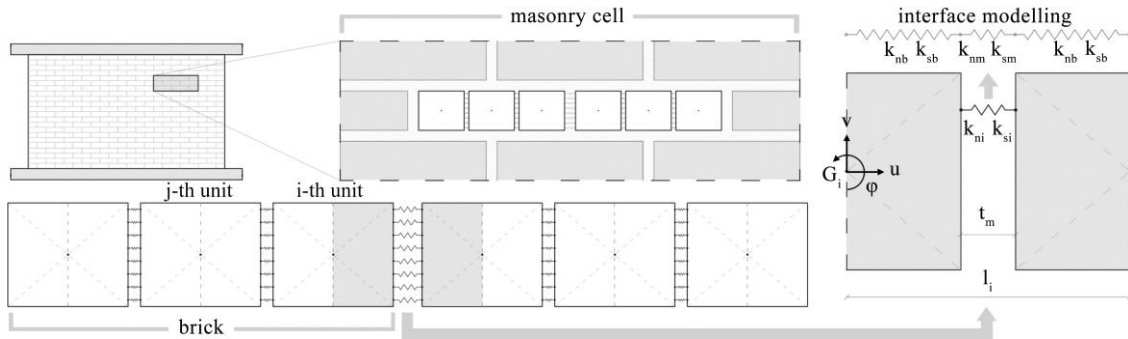


Figure 2. Discretisation of a masonry segment according to the AEM

From a computational viewpoint, two different stiffness matrices are needed here: for the brick elements assembly, since the springs connect elements of identical material, $[K_{bg}]$ is composed of the brick stiffnesses k_{nb} and k_{sb} only, whereas for the interfaces, $[K_{ig}]$ is made up inferring the equivalent stiffnesses k_{ni} and k_{si} (which, as indicated in Figure 2, are obtained assuming the brick and mortar springs arranged in series at an arbitrary contact point).

$$k_{nb} = \left(\frac{E d t_j}{l_j} \right), \quad k_{sb} = \left(\frac{G d t_j}{l_j} \right) \quad (3) \quad \frac{1}{k_{ni}} = \left(\frac{l_i - t_m}{E_b d t_i} + \frac{t_m}{E_m d t_i} \right), \quad \frac{1}{k_{si}} = \left(\frac{l_i - t_m}{G_b d t_i} + \frac{t_m}{G_m d t_i} \right) \quad (4)$$

These parameters, representing the brick-mortar interaction, take into account both the brick and the mortar elastic properties, as shown below. In Eq. (5), the upper left quarter components $[K_{ig/4}]$ of an interface global stiffness matrix $[K_{ig}]$ is reported, where $\Delta \bar{x}_i, \Delta \bar{y}_i$ are the horizontal and vertical relative displacement at the joint level respectively (with reference to the unit centroid), $c = \cos(\varphi)$, and $s = \sin(\varphi)$.

$$[K_{ig/4}] = \begin{bmatrix} k_{ni}(c\varphi)^2 + k_{si}(s\varphi)^2 & (k_{ni} - k_{si})(c\varphi)(s\varphi) & -k_{ni}(c\varphi)(\Delta \bar{y}_i) - k_{si}(s\varphi)(\Delta \bar{x}_i) \\ (k_{ni} - k_{si})(c\varphi)(s\varphi) & k_{si} & -k_{ni}(c\varphi)(\Delta \bar{y}_i) + k_{si}(s\varphi)(\Delta \bar{x}_i) \\ -k_{ni}(c\varphi)(\Delta \bar{y}_i) - k_{si}(s\varphi)(\Delta \bar{x}_i) & -k_{ni}(c\varphi)(\Delta \bar{y}_i) + k_{si}(s\varphi)(\Delta \bar{x}_i) & k_{ni}(\Delta \bar{y}_i)^2 + k_{si}(\Delta \bar{x}_i)^2 \end{bmatrix} \quad (5)$$

In a post-cracked response stage, the elastic parameters implemented in Eq. (5) should be modified according to the material constitutive laws. The AEM employs these criteria changing the stiffness values at each loading step, taking into account the damage evolution; when a given amount of springs has failed and their stiffness is set to zero, contact between units is lost.

2.3 Masonry material models and failure criteria

In this section, the main material models adopted for URM micro-modelling, as well as the failure criteria considered, are described, with particular emphasis on the ones implemented in the AEM. According to the latter, the behaviour of URM structures in the framework of plasticity is modelled considering five different types of allowed failure modes, depicted in Figure 3(a): (1) cracking of the joints, (2) sliding along the bed or head joints, (3) cracking of units in direct tension, (4) diagonal tension cracking of the bricks due to shear-compression and (5) splitting of bricks, [44].

Under these assumptions, it is clear that the first two modes, (1) and (2), should be taken into account by the interface springs, mode (3) should be described by brick springs, and (4) is combined mechanisms involving both interface and brick springs. Failure modes (5) involves both mortar and units. Since the mortar interface is modelled as a zero-thickness interface, and thus the Poisson's effect cannot be included [45], a compressive cap can be implemented to limit the compression stresses in the masonry, according to the behaviour observed under uniaxial testing. The masonry constitutive model typically implemented in AEM codes, for failure modes that come from the joint participation of unit and mortar in high compressive stress, is a linearized version of the "composite interface cap model" proposed in [44] for micro-modelling approaches.

The main objective is to establish an elastic domain bound, introducing numerical operators able to define mathematically each failure mode, i.e. the yield functions. Each failure mode is associated with a pre-defined failure surface. Yielding can only occur if the stresses σ satisfy the general yield criterion $f_i(\sigma, \bar{\sigma}_i(\kappa_i)) = 0$, where the yield stress value $\bar{\sigma}_i$ is a function of a scalar κ_i , which is introduced as a measure for the amount of hardening/softening of i -th yield surface (i.e. plastic deformations) The cap model implemented in the employed AEM code consists of a simplified composite yield criterion with a tension cut-off $f_1(\sigma, \kappa_1) = (\sigma - \bar{\sigma}_1)$, a Coulomb friction model $f_2(\sigma, \kappa_2) = [|\tau| - (\tan(\phi_1)\sigma + \bar{\sigma}_2)]$ and a compressive cap $f_3(\sigma, \kappa_3) = [|\tau| + \tan(\phi_2)(\bar{\sigma}_3 - \sigma)]$, as shown in Figure 3(b).

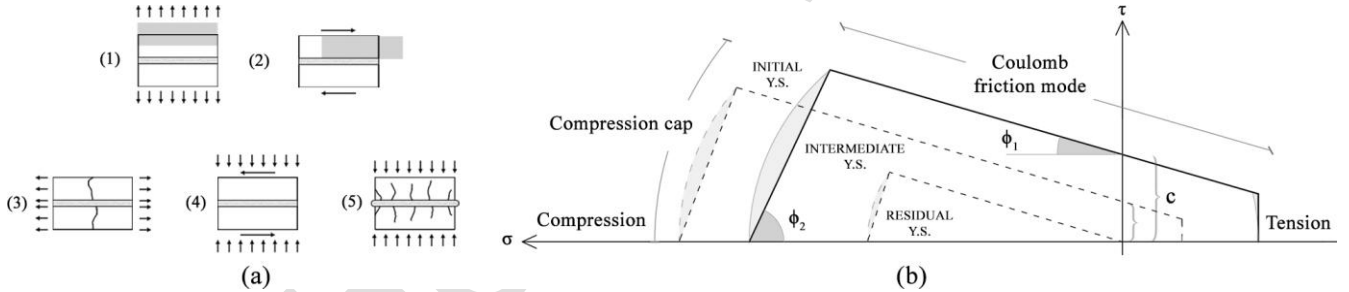


Figure 3. Typical brick-mortar failure mechanisms [44] (a) and composite interface cap model (b)

The yield values are given by Eq. (7) and (8), where f_{tm} is the mortar tensile strength, $\kappa_{1,2,3}$ are the hardening/softening parameters, G_f^I and G_f^{II} the fracture energy of first and second mode, and c is cohesion. Furthermore, ϕ is the interface friction angle, σ_i , σ_p , σ_m , σ_r , κ_m , and κ_p are parameters which can be obtained from uniaxial compression tests of masonry prisms (as reported in [47]). Associate flow rules are adopted for f_1 and f_3 , whereas a non-associate flow rule is considered for f_2 .

$$\bar{\sigma}_1 = \begin{cases} f_{tm} \left(1 - \frac{(f_{tm})(\kappa_1)}{G_f^I} \right), & \kappa_1 \leq \left(\frac{2G_f^I}{f_{tm}} \right) \\ 0, & \kappa_1 > \left(\frac{2G_f^I}{f_{tm}} \right) \end{cases} \quad (7) \quad \bar{\sigma}_2 = \begin{cases} c \left(1 - \frac{(c)(\kappa_2)}{G_f^{II}} \right), & \kappa_2 \leq \left(\frac{2G_f^{II}}{c} \right) \\ 0, & \kappa_2 > \left(\frac{2G_f^{II}}{c} \right) \end{cases} \quad (8)$$

$$\bar{\sigma}_3 = \begin{cases} \bar{\sigma}_a(\kappa_3) = \bar{\sigma}_i + (\bar{\sigma}_p - \bar{\sigma}_i) \left(\frac{2\kappa_3}{\kappa_p} - \frac{\kappa_3^2}{\kappa_p^2} \right)^{-0.5}, & \kappa_3 \leq \kappa_p \\ \bar{\sigma}_b(\kappa_3) = \bar{\sigma}_p + (\bar{\sigma}_m - \bar{\sigma}_p) \left(\frac{\kappa_3}{\kappa_m} - \frac{\kappa_p}{\kappa_m} \right)^2, & \kappa_p < \kappa_3 \leq \kappa_m \\ \bar{\sigma}_c(\kappa_3) = \bar{\sigma}_r + (\bar{\sigma}_m - \bar{\sigma}_r) \left(m \frac{\kappa_3 - \kappa_m}{\bar{\sigma}_m - \bar{\sigma}_r} \right), & \kappa_m < \kappa_3 \end{cases} \quad \text{with} \quad m = 2 \left(\frac{\bar{\sigma}_m - \bar{\sigma}_p}{\kappa_m - \kappa_p} \right) \quad (9)$$

The masonry compressive strength (f_{c_m}) of the cap model follows the hardening/softening law [46] depicted in Figure 4(a). Nevertheless, since each component of masonry is modelled individually (i.e. no homogenised masonry properties like f_{c_m} are considered), an equivalent mortar and brick compressive strength might be introduced (otherwise an early compressive failure of the weakest component might occur, as reported in the following sections) in order to reproduce the masonry compressive response adequately. In this endeavor, rather than altering both the component properties, the mortar compressive strength has been set equal to the one of the brick material. This simplified procedure, which may overestimate the increase of mortar compressive strength due to the confinement effect, has proved to be effective in this specific case, leading to reasonable results. The brick material failure envelope (see Figure 4(b)), instead, is given by the Khoo-Hendry biaxial compressive failure criterion [47] introduced in Eq. (10), where f_{c_b} is the brick compressive strength, f_{c_b}' and f_{t_b}' are the compressive and lateral tensile uniaxial strength of bricks, respectively.

$$\frac{f_{c_b}}{f_{c_b}'} + \left(\frac{f_{t_b}}{f_{t_b}'}\right) \geq 0 \quad (10)$$

$$c = c_0 - \left(\frac{c_0}{G_f^H}\right)(\Delta_{pl}) \quad (11)$$

$$f_{t_m} = f_{t_m} - \left(\frac{f_{t_m}}{G_f^H}\right)(\Delta_{pl}) \quad (12)$$

In the Mohr-Coulomb failure criterion implemented in the AEM code initially developed by Meguro and employed in some of the first numerical applications [46, 48], the cohesion value is assumed constant until the applied strain exceeds the associated yield point, after which it asymptotically decreases. This kind of behaviour is described mathematically by Eq. (11), where c_0 is the initial cohesion and Δ_{pl} is plastic displacement, which mainly depends on the value assigned to the associated fracture energy, G_f^H . The expression proposed in Eq. (11) describes analytically the experimental response observed in several shear tests, as reported in [49]. However, the AEM code employed in this endeavour further simplified this phenomenon by setting the cohesion to zero or eventually assigning a residual cohesion right after the exceedance of the yield point γ_y . Similarly, the bond tensile behaviour shown in Pandey et al. [43] shows a post-peak exponential softening branch, after an initial linear trend, as is clearly shown through Eq. (12) and widely supported by laboratory results [50]. The tensile response of the mortared joint considered for the numerical models proposed in what follows, instead, does not make use of the softening branch. Indeed, once the actual tensile stress exceeds the limit value of f_y , the tensile strength immediately decreases to zero (or to its residual constant value, if specified). In Figure 4 below the abovementioned simplified laws are illustrated, highlighting (dark grey envelopes) the small variations implemented in the current version of the employed AEM code with respect to the original formulation.

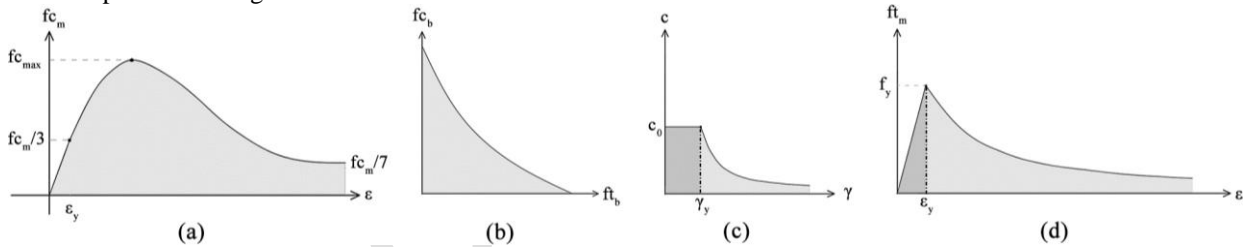


Figure 4. Compressive hardening/softening (a), Khoo-Hendry strength envelope (b), cohesion (c) and bond degradation (d)

Mortared joints, if subjected to shear-compression loading, might exhibit residual shear strength due to the mechanical interaction between mortar and units (i.e. because of the asperity, or roughness, of both the surfaces). This evidence was observed and reported by several authors [51], while no residual cohesion was detected for dry masonry joints during cyclic couplet tests [52]. Numerical applications can be also found in Milosevic et al. [53] and in Parisi and Augenti [54]. The concept of the roughness factor may be mathematically described as the ratio between an actual surface (including material coarseness) and its projection (projected area), as depicted in Figure 5(a). This parameter, mostly used in other fields of mechanics, can be determined empirically (with reference to the technical literature [55]) by means of the Gauckler–Manning–Strickler formulae [56]. At the joint level, it controls the ability of closed cracks to carry shear stress, influencing only the post-cracking behaviour (i.e. when applied stress > shear stress limit). When sliding occurs ($c = 0$), r activates residual frictional resistance by imposing $c \neq 0$ (depending on the level of interface coarseness), as reported in Eq. (13) and illustrated in Figure 5(b):

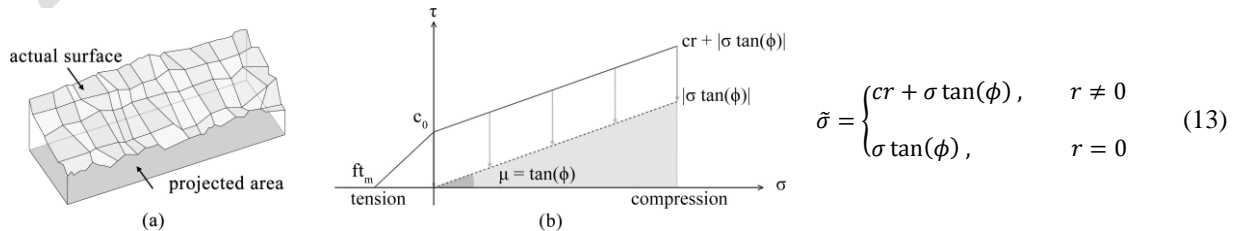


Figure 5. Representation of the roughness mathematical concept (a) and its influence on the Mohr-Coulomb criterion (b)

3. PROPOSED MODEL CALIBRATION PROCESS FOR CALCIUM-SILICATE BRICK MASONRY ELEMENTS

As already mentioned, according to a simplified micro-modelling approach, each component of a masonry element (i.e. bricks and mortar) needs to be described in terms of its mechanical properties. However, experimental campaigns on masonry elements rarely involve tests that would allow one to obtain all necessary material characterisation for brick and mortar separately. This lack of experimental data calls for a pre-processing effort that makes use of empirical formulae available in the literature to obtain first estimates of the aforementioned parameters, as described in the flowchart shown in Figure 6 and 7, below. In addition, and as suggested by Mayorca and Meguro [57], the elastic material properties of mortar need to be subsequently calibrated into equivalent values ($E_{mo,eq}$, $G_{mo,eq}$) that ensue an initial lateral stiffness computed by the model for the URM walls that matches either an expected value for such response parameter (herein termed as “theoretical initial lateral stiffness”, K_{the}) or, if available, the experimentally observed initial lateral stiffness, K_{exp} .

Then, depending on the applied stresses/strains at the joint level, the elastic parameters are adjusted locally by the code according to the implemented material model, in order to reproduce the actual behaviour in the nonlinear range. In summary, one may identify the following four main steps (also schematically represented in the flowcharts of Figure 6 and 7) in the definition/calibration of the material properties for a URM structure to be modelled using the AEM (steps that are herein specified having in mind the case of calcium silicate (CS) brick walls subjected to in-plane cyclic shear-compression tests, which were the modelling target of the current work, for the reasons outline in the Introduction).

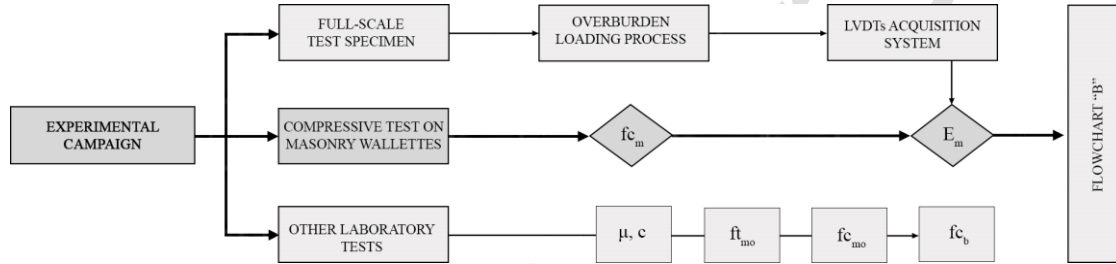


Figure 6. Flowchart A: masonry mechanical properties typically available and of use in a micro-modelling approach

1. *Obtain experimental properties of masonry, bricks and mortar.* The most commonly performed masonry material characterisation tests allow obtaining fundamental modelling parameters such as the compressive strength, the Young’s modulus, the friction coefficient and the cohesion of masonry (fc_m , E_m , μ , c), brick and mortar compressive strength (fc_b , fc_{mo}), and the mortar tensile strength (ft_{mo}). More details about the experimental procedures are reported in section 4.

2. *Infer Young’s and shear modulus of bricks (E_b , G_b) from empirical formulae.* Depending on the brick type, a wide range of empirical relations, founded on experimental outcomes, can be selected. With reference to [58], for CS bricks the Young’s modulus can be estimated using Eq. (14) by multiplying their compressive strength by an experimentally-derived constant:

$$E_b = (fc_b \times 355) \quad (14)$$

3. *Estimate Young’s and shear modulus of mortar (E_{mo} , G_{mo}) from homogenisation formulae.* Since the Young’s modulus of masonry and bricks are known, the Young’s modulus of the mortar can be computed by means of the equations reported in Table I, often employed to develop a homogenisation process. In this work, all four equations described below, where ζ is the ratio of brick’s height to the thickness of mortar joint, were used to infer E_{mo} , and then the ensuing average considered for the models. Furthermore, it is noted that the shear modulus G_{mo} was obtained assuming $G = E/(2(1 + \nu)) = 0.4E$ with $\nu = 0.25$, [59], because no experimental data for this specific parameter were available.

Table I. Derivation of the Young’s modulus of mortar through homogenization criteria

Reference	Homogenisation formulae	Reference	Homogenisation formulae
[60]	$E_{mo} = \left(\frac{-4E_mE_b}{25E_m - 29E_b} \right)$ (15)	[61]	$E_{mo} = \left(\frac{E_mE_b}{E_b - 1.25\zeta(E_m - E_b)} \right)$ (16)
[62]	$E_{mo} = \left(\frac{-E_mE_b}{5E_m - 6E_b} \right)$ (17)	[63]	$E_{mo} = \left(\frac{E_mE_b}{\zeta(E_m - E_b) + E_b} \right)$ (18)

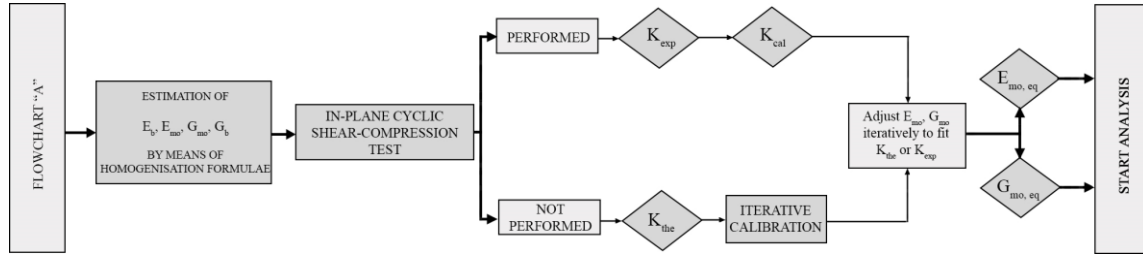


Figure 7. Flowchart B: calibration of equivalent values of E and G for the mortar in URM calcium silicate brick walls

4. Compute K_{the} and iteratively obtain values of equivalent properties of mortar ($E_{mo,eq}$, $G_{mo,eq}$). The “theoretical” initial lateral stiffness of piers can be evaluated for different boundary conditions (i.e. double-fixed, DF, and cantilevered, CL) using the formulae of Eq. (19), where δ is the lateral top displacement which is defined considering both flexural and shear response.

$$\delta_{DF} = \left(\frac{Hh^3}{12E_m} + \frac{Hh}{A_v G} \right), \quad \delta_{CL} = \left(\frac{Hh^3}{3E_m} + \frac{Hh}{A_v G} \right) \quad \text{assuming} \quad \begin{cases} G = 0.4E \\ A = tL \\ A_v = 5/6A \end{cases} \Rightarrow K_{the} = \frac{H}{\delta} = \left(\frac{tE_m}{\left(\frac{h}{L}\right) \left(\omega \left(\frac{h}{L}\right)^2 + 3 \right)} \right) \quad (19)$$

Further, h is the height, L is the length and t is the thickness of the walls, H is the applied horizontal force, E_m is the Young’s modulus of the masonry and A_v is the shear area (equal to 5/6 of the actual lateral one, A). The parameter ω is equal to one in the case of double-fixed boundary conditions, whereas it can be set to four if a cantilevered element is contemplated. Once K_{the} is known, it can then be compared to the initial lateral wall stiffness computed by the uncalibrated AEM model. The values of E_{mo} and G_{mo} are then consequently and iteratively adjusted until the initial lateral stiffness obtained is considered to have reached an acceptable/satisfactory value; such final equivalent mortar E and G values are herein termed $E_{mo,eq}$ and $G_{mo,eq}$. The AEM modelling of the URM post-cracking behaviour is based on the elastic properties degradation, according to the criteria discussed in section 2.3.

4. EXPERIMENTAL CAMPAIGN

A comprehensive experimental campaign was performed by the European Centre for Training and Research in Earthquake Engineering (Eucentre, Pavia, Italy) on mortar/brick specimens (as summarised in Table II) in the period 2014-2016, in the context of a research project on the study of the vulnerability of masonry buildings in Groningen (The Netherlands). In this section, the main testing results for CS brick masonry [64] are briefly reported.

4.1 Masonry characterisation tests

The CS brick masonry walls were characterised by a single leaf periodic arrangement (stretcher bond) of 212 mm x 103 mm x 71 mm units and 10 mm thick mortar joints. The tests illustrated in Figure 8 catered for a wide range of mechanical parameters, however herein only those of relevance for the AEM analysis process are considered and reported in Table II.

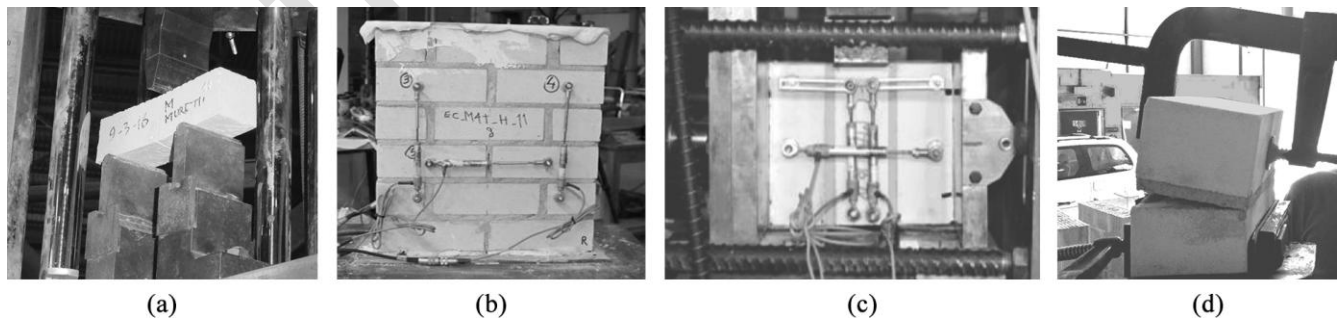


Figure 8. Mortar bending-compression test (a), compression (b), shear (c) and bond wrench test (d) on masonry samples

With reference to the value of E_m reported in Table II below, it was observed that when attempting to calculate it considering each wall overburden σ_v , very similar values of E_{m-2} (i.e. the Young’s modulus of masonry computed as a secant value at 10% of f_{cm}) were obtained for all the piers: for this reason, the latter has been adopted on all the subsequent steps.

Table II. Experimental tests and obtained mechanical properties of CS brick masonry

Experiment	Bending-compression test	Compression test		Triplet test		Bond wrench test
Reference Standard	EN 1015-11	EN 772-1	EN 1052-1	EN-1052-3		EN-1052-5
Material	Mortar	Brick	Masonry			
Obtained property	$f_{c_{mo}}$	f_{c_b}	$E_m (10\%f_{c_m})$	μ	c	$f_{t_{mo}}$
Value [MPa]	5.40	18.67	4182	0.42	0.21	0.24
Specimen type	Prism sample	Halved brick	Walette	Triplet		Two bricks
Specimen number	6	5	6	9		5
Specimen size [mm]	160x40x40	212x103x71	476x434x102	236x212x71		212x103x142
St.Dev. [MPa]	0.19	2.39	1377.97	-		0.04
C.o.V [%]	3.59	13	33	-		16
Density [kg/m ³]	1444	1852	1835			

4.2 In-plane cyclic shear-compression tests on calcium-silicate brick masonry walls

Slender (EC_Comp1, EC_Comp2) and squat (EC_Comp3) full-scale wall specimens were tested in different experimental configurations at the Eucentre laboratory. These piers (shown in Figure 9) were characterised by a single leaf periodic arrangement (stretcher bond) of 212 mm x 103 mm x 71 mm CS units and 10 mm thick mortar joints coming from the same batches used to cast the specimens of the component tests previously described, and built in the same environmental conditions by the same masons.

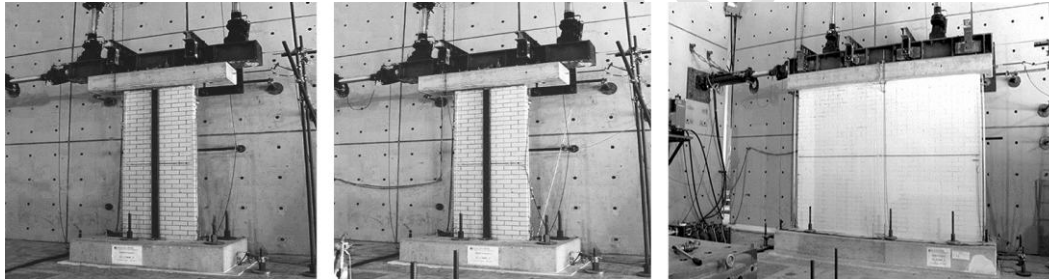


Figure 9. Experimental configurations of the full-scale wall specimens EC_Comp2, EC_Comp1, EC_Comp3

Two different levels of vertical overburden were applied to the slender walls, which featured double fixed boundary conditions, whilst the squat wall was characterised by a cantilever restraint. The geometrical and loading data are reported in Table III below, where h is height, L is length, t is thickness, σ_v is the vertical applied overburden, BC stands for the boundary conditions of the specimens, and OOP refers to out-of-plane.

Table III. Characteristics of the full-scale specimens and their boundary conditions

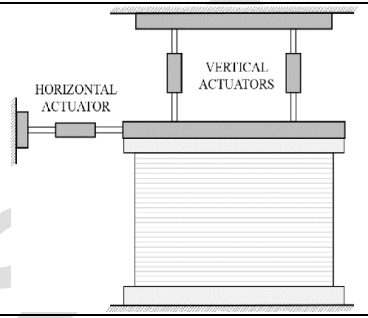
	EC_Comp2	EC_Comp1	BC	EC_Comp3	BC	OOP restraints	
h [mm]	2750	2750		2750		EC_Comp2	EC_Comp1,3
L [mm]	1100	1100		4000			
t [mm]	102	102		102			
σ_v [MPa]	0.70	0.52		0.30			
BC	Double fixed	Double fixed		Cantilever			

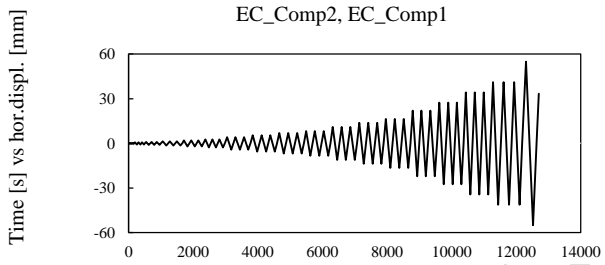
The walls were founded on a reinforced concrete (RC) beam, which is clamped to the lab strong floor with post-tensioned steel bars, whereas the top RC beam, to which the loading was applied, was connected to the masonry piers by means of a layer of self-levelling high strength shrinkage-controlled gypsum to prevent sliding. The top lateral displacements were imposed by a horizontal servo-hydraulic actuator through a steel beam rigidly connected to the RC top-beam. Two horizontal servo-hydraulic actuators assured the boundary conditions, as well as the vertical compression. Furthermore, a restraining system was introduced in order to prevent out-of-plane deflection of the loading beam, as illustrated in Table III. Nevertheless, during the test of the first pier (EC_Comp2), a spurious OOP mechanism was observed and an additional restraint was then

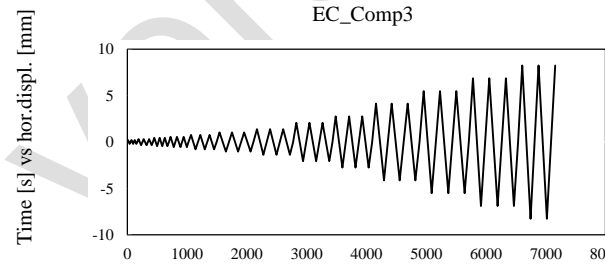
imposed on subsequent tests at the interface between the top RC beam and the walls tested, avoiding a repeat of such unwanted beam rotations and assuring a fully in-plane behaviour. The horizontal top displacement, the vertical and diagonal displacements at the edges of the specimen, the OOP displacements and the force-displacements in the actuators were monitored constantly. For each test, after imposing the vertical top compression, the loading history was applied in a displacement-controlled procedure, as reported in Table IV in terms of target drift. The tests were stopped when the walls lost their bearing capacity or in case of testing problems (e.g. even if the envisaged loading protocol for both the slender piers was the same, the test of EC_Comp2 was interrupted during cycle 8 because of the abovementioned OOP spurious phenomenon).

Table IV. Loading protocol in terms of imposed drift for each cycle [64] and experimental configuration

Cycle	1	2	3	4	5	6	7	8	9
EC_Comp2	0.09	0.33	0.46	0.59	0.84	1.09	1.60	2.10	-
EC_Comp1	0.19	0.26	0.39	0.51	0.76	1.01	1.51	2.02	2.53
EC_Comp3	0.03	0.07	0.10	0.16	0.20	0.28	0.37	0.53	0.81
Cycle	10	11	12	13	14	15	16	17	18
EC_Comp1	3.03	4.04	5.04	6.05	8.06	10.07	12.5	15.0	20.1
EC_Comp3	0.98	1.53	2.06	2.53	3.06	-	-	-	-







4.2.1 EC_Comp2 – slender pier

EC_Comp2 was the first of the quasi-static in-plane tests performed, in double fixed boundary conditions, and featuring an applied average vertical compression of 0.7 MPa. The pier exhibited pure rocking behaviour during the first eight cycles, as gathered from Figure 10(a), without suffering heavy damage. As mentioned above, the originally planned loading protocol was interrupted, due to an OOP failure of the specimen at 0.25% of drift; due to very different in-plane and OOP slenderness of the specimen and insufficient restrain conditions [64], a spurious rotation of the RC top beam was observed (see Figure 10(b)), at 0.15% of drift, with a full-width horizontal crack being formed at the interface between the top course of bricks and the rest of the wall.

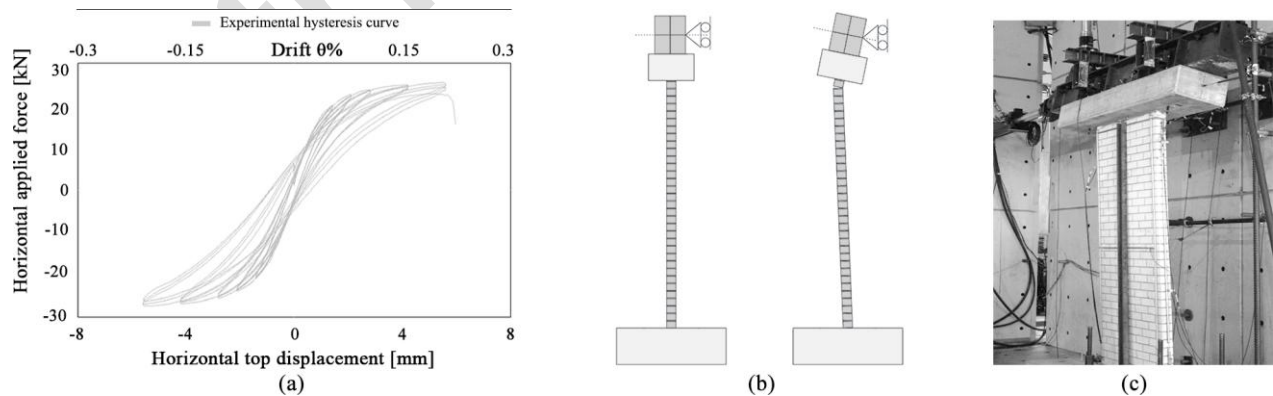


Figure 10. Experimental hysteretic behaviour of EC_Comp2 (a), OOP early failure of the specimen (b), (c)

4.2.2 EC_Comp1 – slender pier

The test performed on EC_Comp1 differed from the previous one just in terms of applied overburden (this time reduced to 0.52 MPa). Furthermore, as already noted, the OOP restraints were enhanced. The loading protocol consisted of eighteen cycles, from a drift of 0.0125% to 2% and from a target displacement of 0.35 mm to 55 mm, characterised by a velocity that

was increased from 0.025 mm/s up to 0.5 mm/s. Together with the hysteretic response, the evolution of the cracks propagation (referred to the most significant cycles) is represented in Figure 11(b):

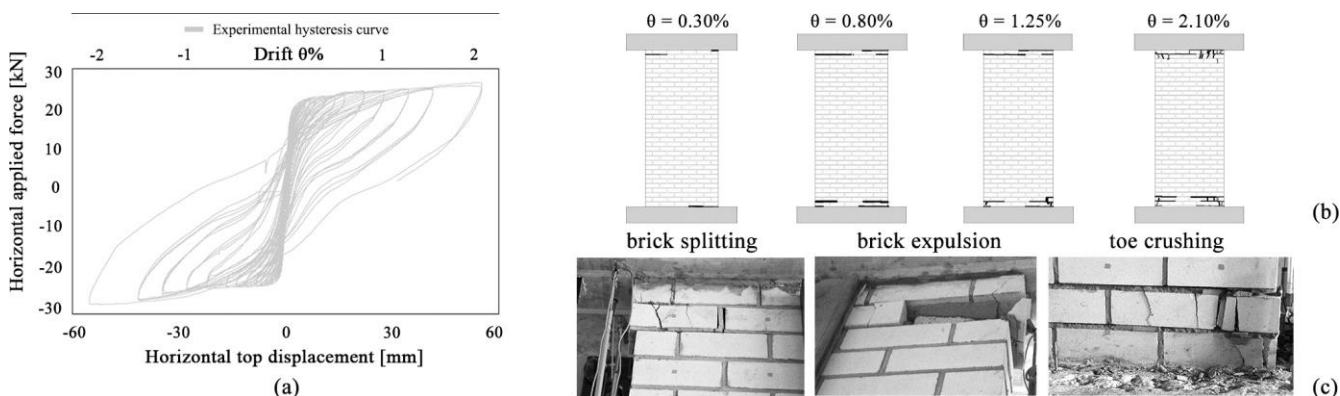


Figure 11. Experimental hysteretic behaviour of EC_Comp1 (a), experimental damage evolution and local failures (b), (c)

The specimen initially exhibited a pure rocking behaviour with horizontal cracks opening at the edges. During the test, new horizontal cracks formed in the next bed-joints, migrating towards the centre of the panel with the effect of shortening the effective height of the wall. This can be also noted in the force-displacement curve reported in Figure 11(a), where a stepped increase of the lateral force is clearly visible due to the different asymptotic flexural strength (rigid body overturning) directly controlled by the modified geometry of the rocking panel. The masonry courses involved in crushing phenomena at the wall toes were not limited to the top and bottom ones, but crushing failures also occurred in several calcium silicate units in the second from top and the second from bottom courses. This contributed to the high energy dissipation exhibited during the test, which is also due to the highly dissipative behaviour of the material in compression as it resulted from material characterization tests [64] and some sliding of the top two courses occurred in the last phases of the test. Cracking pattern at different levels of lateral displacement (drift) and pictures of the damaged specimen are reported in Figure 11(b) and 11(c), respectively.

4.2.3 EC_Comp3 – squat pier

During the test of EC_Comp3, instead, an overburden of 0.3 MPa was imposed. It was characterised by fourteen cycles (the first one conducted in force control), from a drift of 0.025% to 0.3% and from a target displacement of 0.09 mm to 8.25 mm, with a velocity that was increased from 0.015 mm/s up to 0.12 mm/s.

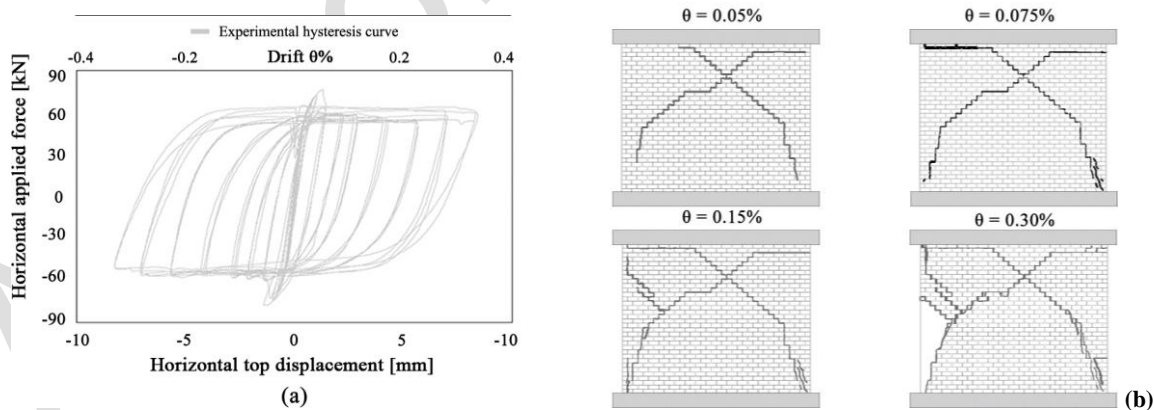


Figure 12. Experimental hysteretic behaviour of EC_Comp3 (a), experimental damage evolution (b)

The specimen exhibited a shear-dominated response, with X stepped cracks forming mainly in the interface between mortar and bricks. The first cracks were developed at a drift of 0.05%. During the higher displacement phase, the deformation of the wall was concentrated always on the same cracks, which therefore saw their width increase. Such cracks widening became even more evident in the last cycles (drift 0.15%), where new diagonal stepped cracks appeared also in the left portion of the wall. This phenomenon is clearly visible in Figure 12(b). Then, the wall continued to concentrate its deformations on the same cracks, which thus saw their width increase up to a partial disaggregation of the mortar joints. This mechanism led to the

partial collapse of the specimen at 0.3% drift. In Figure 13 below, the main observed damages and cracks patterns are documented, whilst in Table V the main experimental data recorded during the tests are reported.

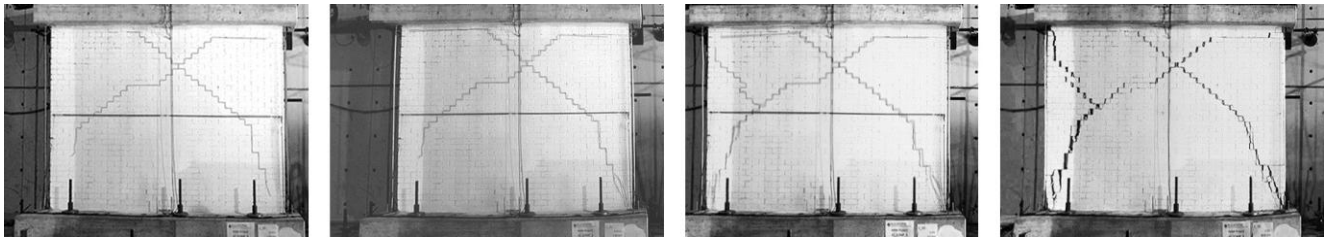


Figure 13. Experimental damage evolution of EC_Comp3

Table V. Summary of the most relevant recorded and inferred data during tests

Specimen	θ_{cr} [%]	V_{max}^+ [kN]	V_{max}^- [kN]	K_{the} [kN/mm]	Dissipated energy [kJ]
EC_Comp2	-	28.6	-24.1	18.4	0.49
EC_Comp1	0.20	26.5	-27.6	18.4	13.73
EC_Comp3	0.05	76.7	-78.0	127.2	14.37

5. SIMULATION OF TESTS ON CALCIUM SILICATE BRICK MASONRY WALLS

5.1 AEM numerical models

The ELS software [65] was used herein. The numerical models of the three URM specimens were characterised by the same modelling approach; a brick mesh-based was initially employed, reproducing the experimental arrangement of units faithfully. An additional discretisation was then applied subdividing the elements along the vertical axis for better capturing the potential brick splitting. Each surface of a given rigid element was connected to the adjacent one by means of twenty-five springs, as depicted in Figure 14 below. The loading and foundation RC beams were explicitly modelled, assuming a linear elastic response with a very high separation strain. As depicted in Figure 14 below, in order to decrease the computational burden, a coarser mesh was assigned to the RC beams; it is noted that the AEM, unlike other methods (such as the FEM), does not need a mesh transition from large-size elements to small elements, since partial connectivity between units is allowed.

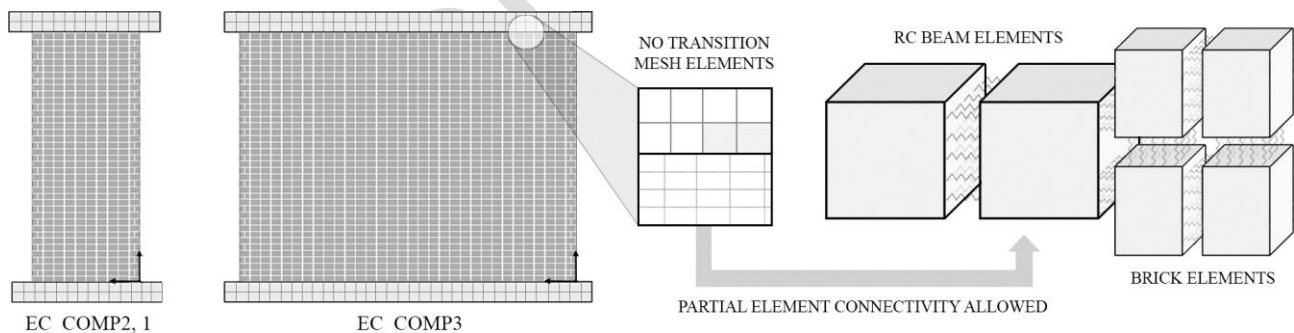


Figure 14. AEM mesh discretisation approach

5.2 Preliminary results obtained with uncalibrated mechanical properties

The values of E and G for brick and mortar as obtained by using the empirical equations reported in points (2) and (3) of section 3 are presented in Table VI.

Table VI. Summary of the inferred material properties of masonry components

E_b [MPa]	G_b [MPa]	E_{mo} [MPa]	G_{mo} [MPa]
6628	2651	1415	566

For the two slender walls (EC_Comp2 and EC_Comp1), the corresponding preliminary AEM models (i.e. models built using the above experimental/inferred material properties, which have not been iteratively calibrated through the procedure proposed in point (4) of section 3) showed initial lateral stiffness (K_{pre}) values that overestimate the experimentally recorded values, as shown in Table VII, below. In addition, these preliminary models exhibited an early collapse (see Figure 15a), due to a premature compressive failure of the mortar interface springs, caused by the fact that the effect of confinement was not considered (i.e. the compressive strength of mortar was used).

For what concerns instead the squat wall (EC_Comp3), the preliminary model showed an initial lateral stiffness K_{pre} that underestimates the experimental recorded value, and exhibited a pure shear behaviour that not properly accounted for the initial rocking mechanisms, thus predicting a shear capacity slightly higher than that of the test specimen (see Figure 15b).

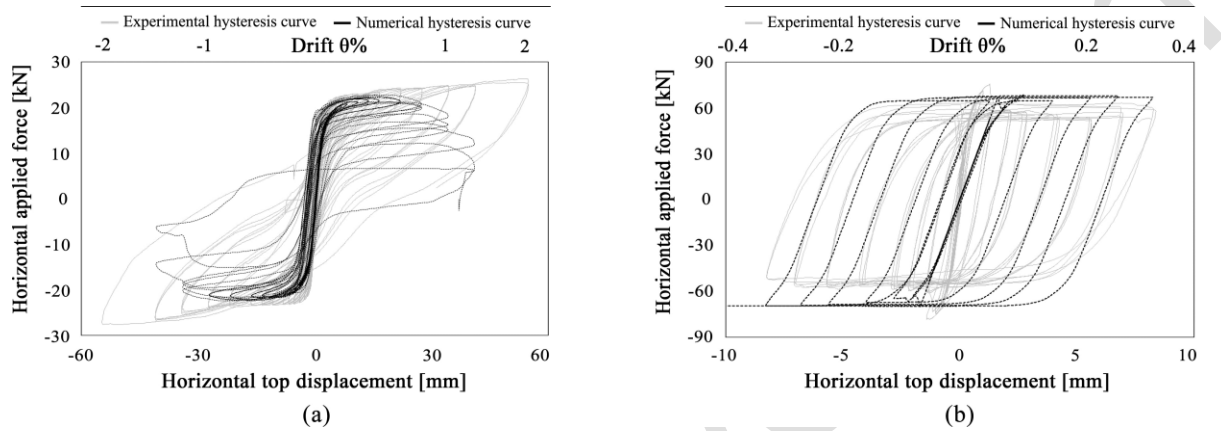


Figure 15. Comparison between preliminary and experimental results of (a) EC_Comp1 and (b) EC_Comp3

5.3 Results obtained with calibrated mechanical properties

The calibration procedure proposed in point (4) of section 3 starts with the computation of the “theoretical” initial lateral stiffness (K_{the}) through the use of Eq. (19), after which values of equivalent E and G for the mortar ($E_{mo,eq}$, $G_{mo,eq}$) are iteratively determined so that the initial lateral stiffness given by the AEM model is similar to K_{the} .

The underlying rationale behind such approach is that K_{the} provides a relatively reliable estimate of the actual stiffness of the masonry wall/pier, notwithstanding the simplified assumptions and approximations that are at the basis of the derivation of Eq. (19), such as e.g.:

- the expression $G = 0.4E$ has inherent variability attached to it
- the value of E_m is not strictly constant, but rather varies as a function of the overburden and deformation level
- actual boundary conditions may differ slightly from perfect cantilever or full-fixity

And indeed, the comparison between the values of “theoretical” and experimental initial lateral stiffness included in Table VII can be considered as relatively satisfactory, with the above limitations in mind. This is reassuring, given that it implies that in those (typical) cases where experimental data is not available, the employed formulae can be used with some degree of confidence. To further demonstrate this point, in the current modelling effort the mortar equivalent material properties were iteratively calibrated against K_{the} , rather than considering K_{exp} (which in this specific case was available and could have been employed).

Table VII. Comparison between theoretical, preliminary and experimental initial lateral stiffness

Specimen	h [mm]	L [mm]	E_m [MPa]	K_{pre} [kN/mm]	K_{exp} [kN/mm]	K_{the} [kN/mm]
EC_Comp2	2750	1100	4182	32.1	24.0	18.4
EC_Comp1	2750	1100	4182	30.4	22.9	18.4
EC_Comp3	2750	4000	4182	102.1	152.4	127.2

5.3.1 EC_Comp2 – slender pier

The Young’s and shear modulus of the mortar, as already mentioned, were iteratively modified until the attainment of a value (numerically-obtained) of initial lateral stiffness (K_{cal}) somewhere in the range of K_{the} , leading to the final properties presented in Table VIII below. The calibrated final results, in terms of hysteretic response, are presented in Figure 16.

Table VIII. Comparison between experimental and calibrated mechanical properties of EC_Comp2

Physical Quantity	Nomenclature	Brick (preliminary = calibrated)	Mortar (preliminary)	Mortar (calibrated)
Specific weight [kg/m ³]	ρ	1852	1444	1444
Tensile strength [MPa]	f_t	1.87	0.28	0.28
Compressive strength [MPa]	f_c	18.67	18.67	18.67
Young's modulus [MPa]	E	6628	1415	4750
Shear modulus [MPa]	G	2651	566	1900
Friction coefficient [-]	μ	0.42	0.42	0.42
Cohesion [MPa]	c	0.21	0.21	0.21
Calibrated initial stiffness [kN/mm]	K_{cal}		22.4	

The analysis was performed according to both the actual loading protocol (Figure 16(a)) and the originally envisaged input sequence (Figure 16(b)), i.e. equal to the one of EC_Comp1, hence beyond the experimental one, stopped due to the spurious rotation of the RC top beam. The numerical outcomes, especially in the very first cycles, seem to approximate relatively well their experimental counterpart. The model capacity is slightly higher compared to the one of the specimen. The dissipated energy by the system during all cycles was computed by identifying the local minima of the Work function and iteratively integrating the area under the curve. The predicted energy dissipation, as depicted in Figure 17 below, is consistently lower. However, since the RC top beam began to rotate at 0.15% of drift (i.e. 4 mm ca), the experimental energy dissipation might have been influenced by the spurious OOP mechanism, increasing its magnitude in the last cycles. Moreover, as observed during the test, no significant damage was predicted by the numerical model (i.e. none of the springs failed). In the final cycles, where no experimental data were available, the energy dissipation increased, due the development of the first cracks along the interfaces with the RC beams (see Figure 16(b)), reaching values similar to EC_Comp1. A lateral strength degradation was also predicted by the model (starting from a displacement of circa 12 mm), due to the cracks migration (the imposed overburden was relatively high) toward the middle portion of the wall.

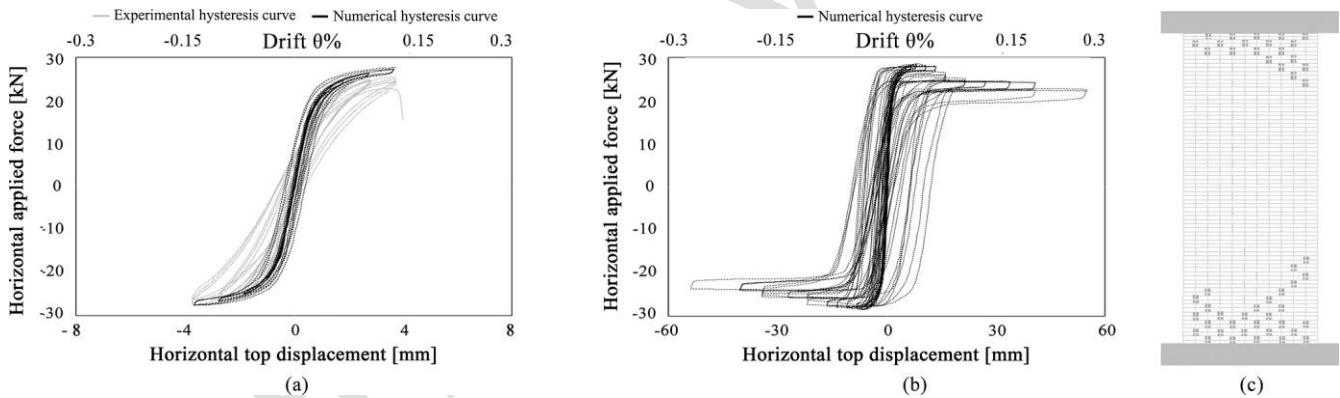


Figure 16. Comparison of experimental and numerical hysteretic behaviour according to both the actual loading protocol imposed to the specimen (a) and the originally planned input sequence (b) of EC_Comp2 with the associated numerical crack pattern (c).

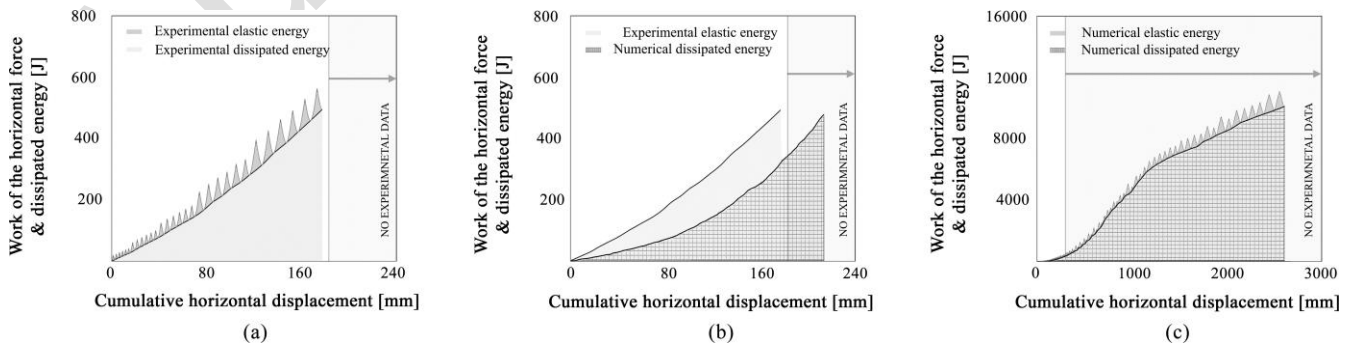


Figure 17. Experimental energy dissipation (a) and numerical vs. experimental (b) energy dissipation of EC_Comp2 related to the actual loading protocol, energy dissipation predicted by the model imposing the initially planned input sequence (c)

5.3.2 EC_Comp1 – slender pier

The EC_Comp1 model, for which the calibrated elastic properties summarised in Table IX were employed, seems to approximate relatively well the capacity of the full-scale specimen, and the global rocking-governed response was adequately captured. Nevertheless, the hysteresis depicted in Figure 18(a) shows some differences with respect to its experimental counterpart in terms of energy dissipation, as evidenced also in Figure 19. This is a common issue in numerical modelling of rocking masonry walls (even using other modelling approaches, e.g. [14]), which is in this case quite evident also due to the unusually high energy dissipation shown by the test of EC_Comp1, as reported in section 4.2. The crack pattern predicted by the model resembles the experimental one though, predicting the experimentally-observed damage at the beam interfaces.

Table IX. Comparison between experimental and calibrated mechanical properties of EC_Comp1

Physical Quantity	Nomenclature	Brick (preliminary = calibrated)	Mortar (preliminary)	Mortar (calibrated)
Specific weight [kg/m ³]	ρ	1852	1444	1444
Tensile strength [MPa]	f_t	1.87	0.28	0.28
Compressive strength [MPa]	f_c	18.67	5.40	18.67
Young's modulus [MPa]	E	6628	1415	4700
Shear modulus [MPa]	G	2651	566	1880
Friction coefficient [-]	μ	0.42	0.42	0.42
Cohesion [MPa]	c	0.21	0.21	0.21
Calibrated initial stiffness [kN/mm]	K_{cal}		21.3	

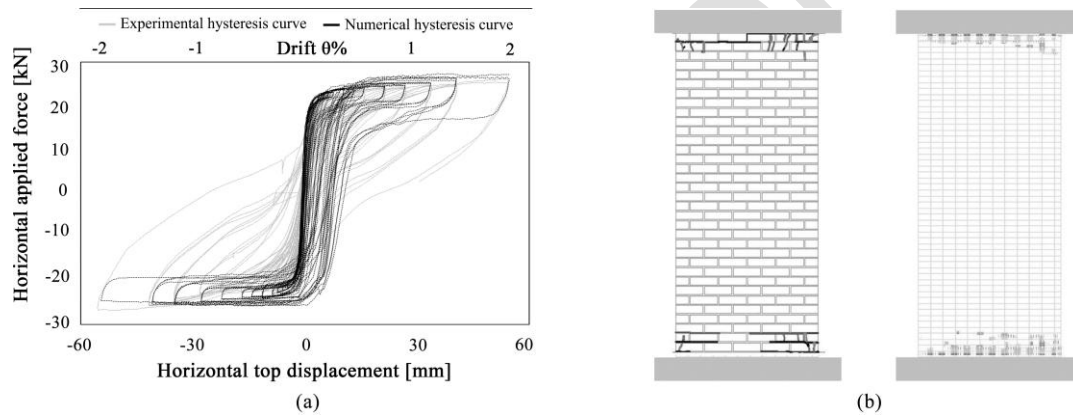


Figure 18. Comparison of experimental and numerical hysteretic behaviour (a) and numerical vs. experimental crack pattern (b) of EC_Comp1

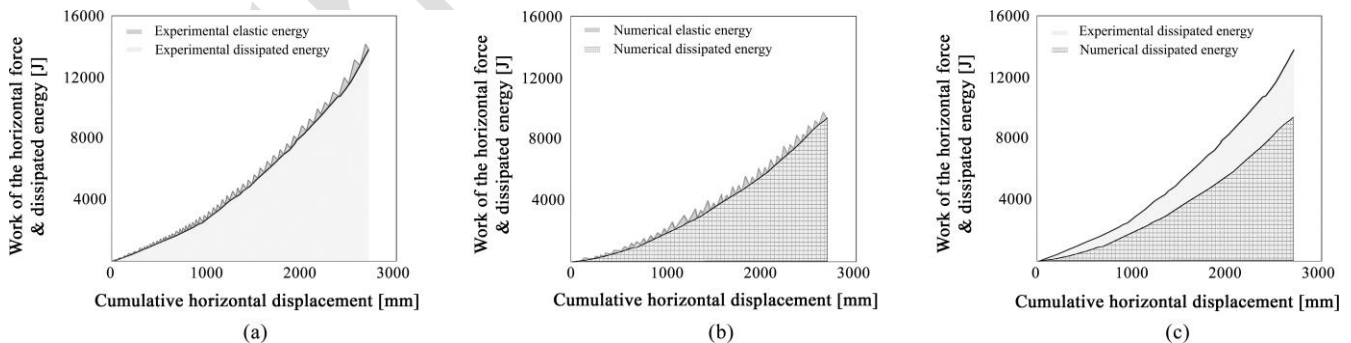


Figure 19. Experimental (a), numerical (b) and compared (c) energy dissipation of EC_Comp3

5.3.3 EC_Comp3 – squat pier

EC_Comp3 was the last CS masonry pier tested in-plane during this experimental campaign. The calibrated elastic parameters are reported in Table X. The numerical model seems to reproduce adequately the global response of EC_Comp3, both in terms of capacity and stiffness. The predicted behaviour, if compared to the experimental one, is characterised by a more pronounced rocking-bending response of the first cycles, whilst the pure shear mechanism starts afterwards, with lower dissipated energy. Indeed, the crack pattern does not represent the experimental X-stepped cracks development accurately,

even if the overall response was captured (see Figure 20). A failure of the interface between both the top and the bottom RC beams was observed during the first cycles, whilst a migration of the cracks from the bottom to the upper portion of the pier was detected afterwards.

Table X. Comparison between experimental and calibrated mechanical properties of EC_Comp3

Physical Quantity	Nomenclature	Brick (preliminary = calibrated)	Mortar (preliminary)	Mortar (calibrated)
Specific weight [kg/m ³]	ρ	1852	1444	1444
Tensile strength [MPa]	ft	1.87	0.28	0.28
Compressive strength [MPa]	fc	18.67	5.40	18.67
Young's modulus [MPa]	E	6628	1415	4500
Shear modulus [MPa]	G	2651	566	1800
Friction coefficient [-]	μ	0.42	0.42	0.42
Cohesion [MPa]	c	0.21	0.21	0.21
Calibrated initial stiffness [kN/mm]	K_{cal}		144.2	

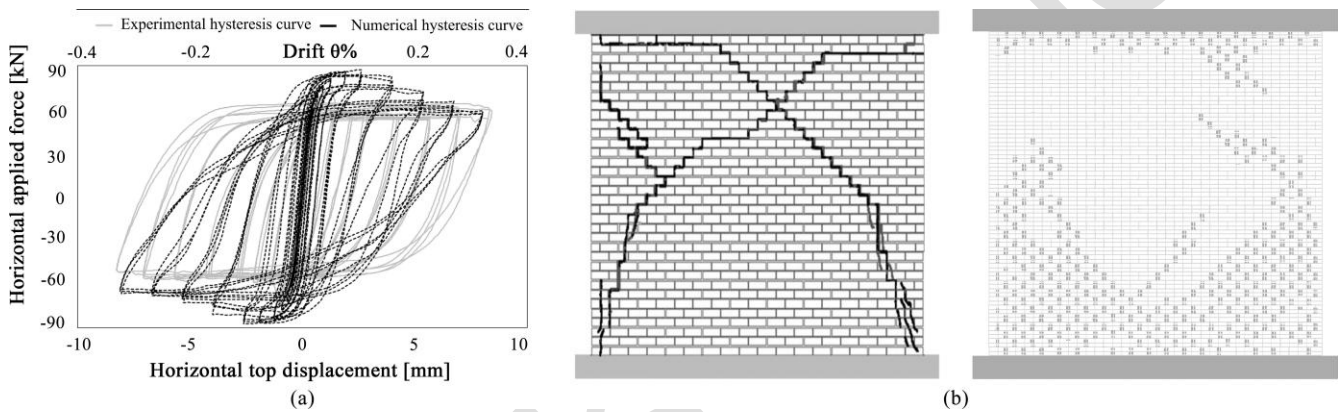


Figure 20. Comparison of experimental and numerical hysteretic behaviour (a) and experimental vs. numerical crack pattern (b) of EC_Comp3

The energy dissipation prediction is accurate, especially in the first phase of the test (i.e. until a cumulative displacement of circa 270 mm, corresponding to the end of the 11th cycle), as shown in Figure 21 (c). At the end of the test, instead, the gap between the numerical and experimental energy dissipation increases up to a final value of 1.52 kJ. This is mainly ascribable to the different crack pattern exhibited by the model, associated to a structural behavior governed by flexural failure modes in the first cycles.

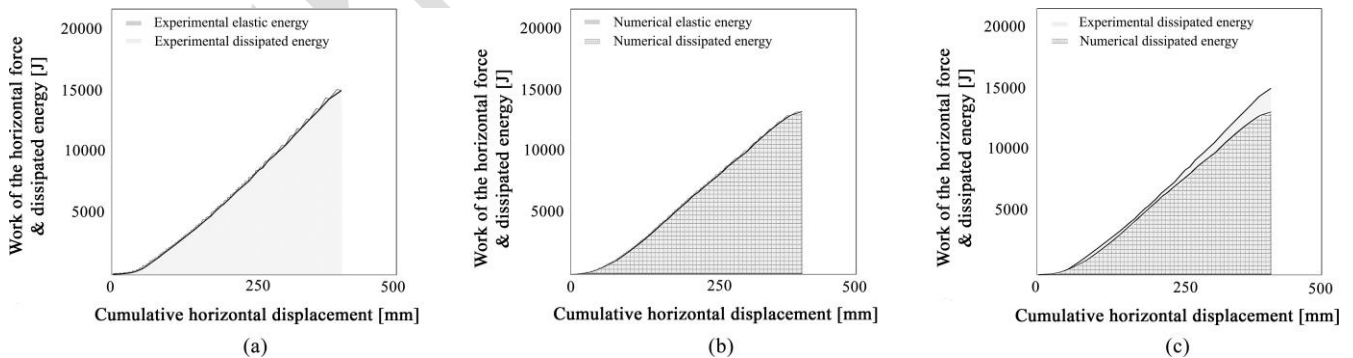


Figure 21. Experimental (a), numerical (b) and compared (c) energy dissipation of EC_Comp3

It is noted that, as shown in [43], the numerical predictions for this specimen, and in particular that of the crack pattern, could be improved further by empirically adjusting some of the material parameters, an option that however was not explored in this paper, where the objective is that of describing a modelling strategy that can be readily applied to the general case of when no experimental results are available.

6. CONCLUSIONS

The Applied Element Method (AEM) is a modelling technique based on the mechanical interaction between rigid bodies, which are connected by means of spring layers, where the material properties are lumped. The AEM was already employed in some applications concerning the simulations of URM structures (mostly large-scale buildings not experimentally tested), as well as the in-plane quasi-static response of URM components. Nevertheless, the mechanical performance of calcium silicate brick masonry has never been investigated using this numerical approach. Moreover, neither a specific calibration procedure nor a careful validation against a series of experimental results is currently available in literature. The latter highlighted the advantages of a proper adjustment of the initial material properties assigned to the spring interfaces, through a methodology that is applicable to the general and common case of when no experimental results are available.

In this endeavour thus, the numerical prediction of the in-plane cyclic response of calcium-silicate walls using the AEM was discussed and scrutinised, through comparison against laboratory test results. Validation of this numerical approach was undertaken by an attempt to reproduce the results of in-plane shear-compression tests on three full-scale calcium-silicate masonry wall specimens.

For the definition of the material mechanical properties of brick and mortar, a pre-processing methodology, founded on theoretical and empirical techniques able to infer such physical quantities, was elaborated. For this purpose, several expressions (mainly referred to the masonry homogenisation theory) were considered and reviewed, showing how some masonry properties (i.e. Young's and shear modulus of mortar) can be iteratively and readily calibrated to enhance the modelling results, even in the nonlinear range. Moreover, it is worth noting the advantages of a "global" calibration method (e.g. considering the wall lateral stiffness as a target parameter rather than local-scale physical quantities), whereby the additional modelling of characterisation tests is not necessarily needed.

The AEM models presented in this work captured with varying levels of accuracy the hysteretic response, the energy dissipation and the crack patterns of the test specimens. The results, whilst relatively satisfactorily as a whole, also showed that improvements are warranted. Such possible enhancements are currently being explored, as is the extension and verification of this modelling approach to different loading conditions (including out-of-plane dynamic loading) and more complex structures.

ACKNOWLEDGMENTS

The work described in this paper was carried out within the framework of the research programme on hazard and risk of induced seismicity in the Groningen region, sponsored by the Nederlandse Aardolie Maatschappij BV (NAM). The authors also acknowledge all those at the European Centre for Training and Research in Earthquake Engineering (EUCENTRE, Pavia, Italy) that were involved in the testing campaign referred to in this paper, as well as the technical support staff from Applied Science International LLC (ASI), for the guidance on the use of the employed AEM software - Extreme Loading for Structures. Finally, the authors would like to express their gratitude to Prof. Ferdinando Auricchio (University of Pavia, Italy), for his support in the investigation of the theoretical aspects of the AEM, and to two anonymous reviewers, whose detailed and constructive feedback contributed to a significant improvement of the overall quality of this manuscript.

REFERENCES

1. Bourne SJ, Oates SJ, Bommer JJ, Dost B, van Elk J, Doornhof D. A Monte Carlo method for probabilistic hazard assessment of induced seismicity due to conventional natural gas production. *Bulletin of the Seismological Society of America*, 2015; **105**(3): 1721-1738.
2. Bommer, JJ, van Elk J. Comment on "The maximum possible and the maximum expected earthquake magnitude for production-induced earthquakes at the gas field in Groningen, The Netherlands" by Gert Zöller and Matthias Holschneider. *Bulletin of the Seismological Society of America*, 2017; **107**(3):1564-1567.
3. Graziotti F, Tomassetti U, Kallioras S, Penna A, and Magenes G. Shaking table test on a full scale URM cavity wall building. *Bulletin of Earthquake Engineering*, 2017; **15**(12): 5329-5364. DOI: <https://doi.org/10.1007/s10518-017-0185-8>.
4. Heyman, J. The stone skeleton. *International Journal of Solids and Structures* 1966; **2**(2):249-279.
5. D'Ayala D, Speranza E. Definition of collapse mechanisms and seismic vulnerability of historic masonry buildings. *Earthquake Spectra* 2003; **19**(3): 479-509. DOI: 10.1193/1.1599896.
6. Block P, Ciblac T, Ochsendorf J. Real-time limit analysis of vaulted masonry buildings. *Computers & Structures* 2006; **84**(29-30):1841-1852. DOI: 10.1016/j.compstruc.2006.08.002.
7. Braga F, Dolce, M (1982). *A method for the analysis of antiseismic masonry multi-storey buildings*, in *Proceedings of 16th International Brick and Block Masonry Conference*: Roma, Italy.
8. Tomaževič M. Dynamic modelling of masonry buildings: storey mechanism model as a simple alternative. *Earthquake Engineering & Structural Dynamics* 1987; **15**(6):731-749. DOI: 10.1002/eqe.4290150606.

9. Graziotti, F, Penna, A, Magenes G. A nonlinear SDOF model for the simplified evaluation of the displacement demand of low-rise URM buildings. *Bulletin of Earthquake Engineering* 2016, **14**(6):1589-1612. DOI: 10.1007/s10518-016-9896-5.
10. DeJong MJ, Dimitrakopoulos EG. Dynamically equivalent rocking structures. *Earthquake Engineering & Structural Dynamics* 2014; **43**(10):1543-1563. DOI: 10.1002/eqe.2410.
11. Costa AA, Penna A, Arède A, Costa A. Simulation of masonry out-of-plane failure modes by multi-body dynamics. *Earthquake Engineering & Structural Dynamics* 2015; **44**(14):2529-2549. DOI: 10.1002/eqe.2596.
12. Chen SY, Moon FL, Yi T. A macroelement for the nonlinear analysis of in-plane unreinforced masonry piers. *Engineering Structures* 2008; **30**(8):2242-2252. DOI: 10.1016/j.engstruct.2007.12.001.
13. Lagomarsino S, Penna A, Galasco A, Cattari S. TREMURI program: an equivalent frame model for the nonlinear seismic analysis of masonry buildings. *Engineering Structures* 2013; **56**:1787-1799. DOI: 10.1016/j.engstruct.2013.08.002.
14. Penna A, Lagomarsino S, Galasco A. A nonlinear macroelement model for the seismic analysis of masonry buildings. *Earthquake Engineering & Structural Dynamics* 2014; **43**(2):159-179. DOI: 10.1002/eqe.2335.
15. Addessi D, Mastrandrea A, Sacco E. A force-based equivalent frame element for push-over analysis of masonry structures. *Key Engineering Materials* 2015; **624**:405-412. DOI: 10.4028/www.scientific.net/KEM.624.405.
16. Raka E, Spacone E, Sepe V, Camata G. Advanced frame element for seismic analysis of masonry structures: model formulation and validation. *Earthquake Engineering & Structural Dynamics* 2015; **44**(14):2489-2506. DOI: 10.1002/eqe.2594.
17. Roca P, Cervera M, Gariup G, Pelà L. Structural analysis of masonry historical constructions. Classical and advanced approaches. *Archives of Computational Methods in Engineering* 2010; **17**(3):299-325.
18. Cundall, PA (1971). *A computer model for simulating progressive large scale movements in blocky rock systems*. in *Symposium of Rock Fracture (ISRM)*: Nancy, France.
19. Lemos JV. Discrete element modeling of masonry structures. *International Journal of Architectural Heritage* 2007; **1**(2):190-213. DOI: 10.1080/15583050601176868.
20. Bakeer, TT. *Collapse analysis of masonry structures under earthquake actions*. in *Bauforschung und Baupraxis*, Publication series of the Chair of Structural Design of the Dresden University of Technology, Germany, 2009; **8**:70-76.
21. Cundall PA, Hart RD. Numerical modelling of discontinua. *Engineering Computations* 1992; **9**(2):101-113. DOI: 10.1108/eb023851.
22. Lourenço PB. Computations on historic masonry structures. *Progress in Structural Engineering and Materials* 2002; **4**(3):301-319.
23. De Lorenzis L, DeJong MJ, Ochsendorf J. Failure of masonry arches under impulse base motion. *Earthquake Engineering & Structural Dynamics*, 2007; **36**(14):2119-2136. DOI: 10.1002/eqe.719.
24. Tondelli M, Beyer K, DeJong MJ. Influence of boundary conditions on the out-of-plane response of brick masonry walls in buildings with RC slabs. *Earthquake Engineering & Structural Dynamics*, 2016; **45**(8):1337-1356. DOI: 10.1002/eqe.2710.
25. Goodman, R. E. (1988). *Discontinuous deformation analysis: a new method for computing stress, strain and sliding of block systems*. in *Symposium on Rock Mechanics (USRMS)*: Minneapolis, USA.
26. Jean M. The non-smooth contact dynamics method. *Computer Methods in Applied Mechanics and Engineering*, 1999; **177**(3-4):235-257.
27. Moreau JJ. Unilateral contact and dry friction in FFD, *Nonsmooth Mechanics and Applications*, 1988; **302**:1-82.
28. Chetouane B, Dubois F, Vinches M., Bohatier C. NSCD discrete element method for modelling masonry structures, *International Journal for Numerical Methods in Engineering*, 2005; **64**(1):65-94.
29. Portioli F, Cascini, L. Contact dynamics of masonry block structures using mathematical programming. *Journal of Earthquake Engineering*, 2016; 1-32.
30. Rafiee A, Vinches, M, Bohatier C. Application of the NSCD method to analyse the dynamic behaviour of stone arched structures. *International Journal of Solids and Structures*, 2008; **45**(25-26):6269-6283. DOI: 10.1016/j.ijsolstr.2008.07.034.
31. Rafiee A, Vinches, M, Bohatier C. Modelling and analysis of the Nîmes arena and the Arles aqueduct subjected to a seismic loading, using the Non-Smooth Contact Dynamics method. *Engineering Structures*, 2008; **30**(12):3457-3467. DOI: 10.1016/j.engstruct.2008.05.018.
32. Gu X, Zhang J, Jia X, Chen L, Chen G (2016). *Multi-scale analysis of masonry structures based on discrete element method*, in *Proceedings of 16th International Brick and Block Masonry Conference Masonry*: Padua, Italy.
33. Kawai T. New discrete models and their application to seismic response analysis of structures. *Nuclear Engineering and Design*, 1978; **48**(1):207-229.
34. Casolo S. Modelling the out-of-plane seismic behaviour of masonry walls by rigid elements. *Earthquake Engineering and Structural Dynamics*, 2000; **29**(12):1797-1813. DOI:10.1002/1096-9845(200012)29:12<1797::AID-EQE987>3.0.CO;2-D
35. Meguro K, Tagel-Din H. Applied element method for structural analysis: Theory and application for linear materials. *JSCE Structural Engineering/Earthquake Engineering*, 2000; **17**(1):21-35.
36. Casolo S. Macroscale modelling of microstructure damage evolution by a rigid body and spring model. *Journal of Mechanics of materials and Structures*, 2009, **4**(3):551-570.
37. Tagel-Din H, Meguro K. Consideration of Poisson's ratio effect in structural analysis using elements with three degrees of freedom. *Bulletin of Earthquake Resistant Struct. Res. Ctr*, 1998; **31**(1):41-50.
38. Casolo S, Pena F. Rigid element model for in-plane dynamics of masonry walls considering hysteretic behaviour and damage. *Earthquake Engineering and Structural Dynamics*, 2007; **36**(8):1029-1048. DOI: 10.1002/eqe.670
39. Karbassi A, Nollet MJ. Performance-based seismic vulnerability evaluation of masonry buildings using Applied Element Method in a nonlinear dynamic-based analytical procedure. *Earthquake Spectra*, 2013; **29**(2):399-426. DOI: 10.1193/1.4000148.
40. Furukawa A, Kiyono J, Toki K. Numerical simulation of the failure propagation of masonry buildings during an earthquake. *Journal of Natural Disaster Science*, 2012; **33**(1):11-36.

41. Meguro K., Tagel-Din H. Applied Element simulation of RC Structures under cyclic loading. *ASCE Journal of Structural Engineering* 2001; **127**(11):1295-1305.
42. Meguro K., Tagel-Din H. Applied Element Method used for large displacement structure analysis. *Journal of Natural Disaster Science*; **24**(2):65-82.
43. Malomo D, Pinho R (2016). AEM modelling of URM walls subjected to in-plane cyclic shear-compression using Extreme Loading for Structures. Modelling Report, Mosayk, Pavia, Italy.
44. Lourenco PB, Rots JG, Blaauwendraad J. Two approaches for the analysis of masonry structures: micro and macro-modeling. in *Heron*, Publication series of the Built Environment and Geosciences Department of the Delft University of Technology, The Netherlands, 1995; **40**(4):314-343.
45. Asteris PG, Sarhosis V, Mohebkhah A, Plevris V, Papaloizou mL, Komodromos P, & Lemos JV (2015). Numerical modeling of historic masonry structures. in *Handbook of Research on Seismic Assessment and Rehabilitation of Historic Structures*, 213-256. DOI: 10.4018/978-1-4666-8286-3.ch007
46. Pandey BH, Meguro K (2004). *Simulation of brick masonry wall behavior under in plane lateral loading using applied element method*, in *Proceedings of the 13th World Conference on Earthquake Engineering*: Vancouver, Canada.
47. Khoo CL, Hendry AW (1973). *Strength tests on brick and mortar under complex stresses for the development of a failure criterion for brickwork in compression*, in *Proceedings of the British Ceramic Society*, **21**.
48. Guargain R, Worakananchana K, Mayorca P, Meguro K. Simulation of brick masonry wall behavior under cyclic loading using applied element method. in *Seisan Kenkyu*, Journal of the Institute of Industrial Science of the University of Tokyo, Japan, 2006; **58**(6):531-534.
49. Van Zijl G (1996). Shear transfer across bed joints in masonry: A numerical study. *TU-DELFT Technical report*, 03.21:0.22, Delft University of Technology, The Netherlands.
50. Hordijk DA. (1991). Local approach to fatigue of concrete. PhD Thesis, Delft University of Technology, The Netherlands.
51. Van der Pluijm R (1993). *Shear behaviour of bed joints*, in *Proceedings of the 6th North American Masonry Conference*, Philadelphia, USA.
52. Lourenço PB, Ramos LF. Characterization of the cyclic behavior of dry masonry joints, *Journal of Structural Engineering*, ASCE, 2004; **130**(5):779-786.
53. Milošević J, Gago AS, Lopes M and Bento R (2012). Triplet test on rubble stone masonry panels, in *Proceedings of the 15th World Conference on Earthquake Engineering*: Lisbon, Portugal.
54. Parisi F, Augenti N (2012). A shear response surface for the characterization of unit-mortar interfaces, in *Proceedings of the 15th International Brick and Block Masonry Conference*, Brazil.
55. Belem T, Homand-Etienne F, Souley M. Quantitative parameters for rock joint surface roughness. *Rock Mechanics and Rock Engineering*, 2000; **33**(4):217-242.
56. Manning R, Griffith JP, Pigot TF, Vernon-Harcourt LF. *On the flow of water in open channels and pipes*. Institute of Civil Engineers of Ireland Transactions: Dublin, Ireland, 1890.
57. Mayorca P, Meguro K. Modeling masonry structures using the applied element method, in *Seisan Kenkyu*, Journal of the Institute of Industrial Science of the University of Tokyo, Japan, 2003; **55**:581-584.
58. Irmschler HJ, Schubert P, Jäger W. in *Mauerwerk-Kalender*, 2004; Ernst & Sohn: Berlin, Germany.
59. Lekhnitskii SG. *Theory of elasticity of an anisotropic elastic body*. Holden-Day: San Francisco, USA.
60. Brooks JJ, Baker A. Modulus of elasticity of masonry. *Masonry International*, 1998; **12**:58-63.
61. Matysek P, Janowski Z (1996). *Analysis of factors affecting the modulus of elasticity of the walls*, in *Proceedings of the Conference of the Committee of Civil Engineering PZITB*: Lublin, Poland. [in Polish]
62. Ciesielski R (1999). The dynamic module of elasticity of brick walls, in *Proceedings of the Conference of the Committee of Civil Engineering PZITB*: Wrocław-Krynica, Poland. [in Polish]
63. International Conference of Building Officials (1991), Uniform Building Code, Whittier, USA.
64. Graziotti F, Rossi A, Mandirola M, Penna A, Magenes G (2016). *Experimental characterization of calcium-silicate brick masonry for seismic assessment*, in *Proceedings of 16th International Brick and Block Masonry Conference* Masonry: Padua, Italy.
65. ASI (2017). Extreme Loading for Structures v5, Applied Science International LLC., Durham, USA.